Optics Letters

3D porous graphene-assisted capsulized cholesteric liquid crystals for terahertz power visualization

Lei Wang,[1,2,5] Ruiwen Xiao,[2] Shengxin Yang,[3] Hongsong Qiu,[3] Zhixiong Shen,[1] Peng Lv,[2] Caihong Zhang,[3] Wei Hu,[1] Makoto Nakajima,[4] Biaobing Jin,[3] and Yanqing Lu[1,*]

[1]National Laboratory of Solid State Microstructures, Key Laboratory of Intelligent Optical Sensing and Manipulation, and College of Engineering and Applied Sciences, Nanjing University, Nanjing 210093, China
[2]College of Electronic and Optical Engineering & College of Microelectronics, Nanjing University of Posts and Telecommunications, Nanjing 210023, China
[3]Research Institute of Superconductor Electronics (RISE), School of Electronic Science and Engineering, Nanjing University, Nanjing 210093, China
[4]Institute of Laser Engineering, Osaka University, Suita, Osaka 565-0871, Japan
[5]e-mail: wangl@njupt.edu.cn
*Corresponding author: yqlu@nju.edu.cn

Received 18 August 2020; accepted 22 September 2020; posted 24 September 2020 (Doc. ID 405695); published 15 October 2020

We demonstrate a high-efficiency visualized terahertz (THz) power meter based on the THz-photothermochromism of capsulized cholesteric liquid crystals (CCLCs) embedded in three-dimensional porous graphene (3DPG). The graphene is a broadband perfect absorber for THz radiation and transfers heat efficiently, and its black background is beneficial for color measurement. Quantitative visualization of THz intensity up to 2.8×10^2 mW/cm^2 is presented. The minimal detectable THz power is 0.009 mW. With multi-microcapsule analysis, the relationship between THz power and the average hue value of CCLCs achieves linearity. The device can convert THz radiation to visible light and is lightweight, cheap, and easy to use.

https://doi.org/10.1364/OL.405695

Terahertz (THz) radiation, which lies in the electromagnetic spectrum from 0.1 to 10 THz, has very useful properties and numerous applications [1–4]. Because THz frequency is much higher than the cutoff frequency of traditional electronic devices and its photo energy is much lower than the bandgap of conventional semiconductor materials, it is difficult to detect THz waves effectively using common electronic and optical methods. The lack of THz detectors with high sensitivity, fast response, and easy integration seriously restricts the application of THz technology at ambient temperature. The thermal detection mechanism, based on certain temperature-related physical property changes caused by THz radiation, is not limited by material bandgap, and can detect wideband THz radiation, so it has become the most direct and conventional THz detection method. Conventional THz thermal detectors are typically based on electronic information, and require complex fabrication and are bulky and expensive [5–7]. The Golay detector can measure THz radiation through the optical method, but it exhibits low efficiency and poor practicability [8]. THz beam spot size has also been directly measured by a commercial charge-coupled device (CCD) camera [9]. The challenge of making THz detectors high efficiency, low cost, and easy to use remains.

In order to meet the requirement of high efficiency and practicality, visualized THz detectors based on the thermochromic effect of cholesteric liquid crystal (CLC) have been developed [10,11]. In this kind of detector, the temperature rise caused by incident THz waves shortens the helical pitch of the CLC, causing vivid color changes. The power of the THz irradiation can be obtained by quantifying the hue of the visible light of the CLC, which does not require electronic devices, power supplies, or connecting cables. Tadokoro *et al*. designed a sensor card with CLCs for THz beam profile in 2015 [12]. However, due to the limitation of THz absorptivity, the detected THz power density must be greater than 4.3 mW/cm^2. In 2018, we used a CLC film to achieve a quantitative visualization of THz intensity up to 4.0×10^3 mW/cm^2. The detectable THz field threshold was 0.07 mW, but the maximum absorption of THz radiation by the CLC film in the frequency range of 0.5–1.5 THz was still about 60% [13]. Kang *et al*. combined metamaterial with CLC to detect THz power [14], but the heat induced by THz radiation is difficult to use to heat CLC effectively.

A highly efficient THz absorber and an active THz shielding (from 0.1–1.2 THz) based on 3D graphene foam have been reported [15,16]. Using this kind of graphene, a new kind of THz detector based on the photothermoelectric effect has been presented [17]. Three-dimensional porous graphene (3DPG) has ultra-wideband photon absorption, excellent photothermal

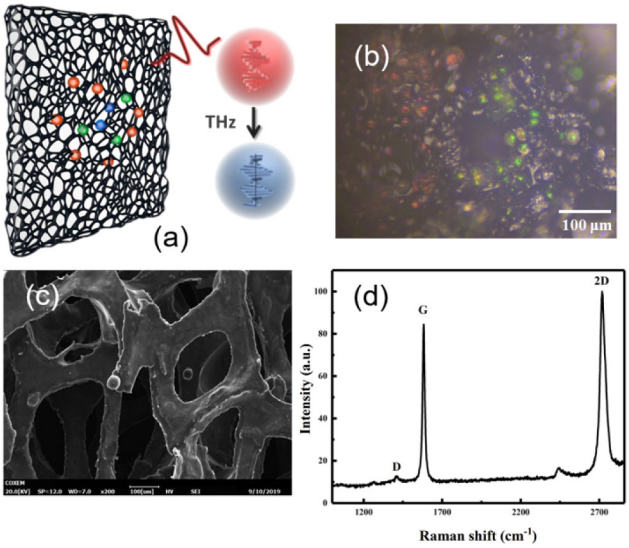

Fig. 1. Characteristics of three-dimensional porous graphene (3DPG) with embedded capsulized cholesteric liquid crystals (CCLCs). (a) Schematic and principle of the components. (b) Microscopic image. (c) Scanning electron microscopy (SEM) image of 3DPG with CCLCs. (d) Raman spectrum of 3DPG.

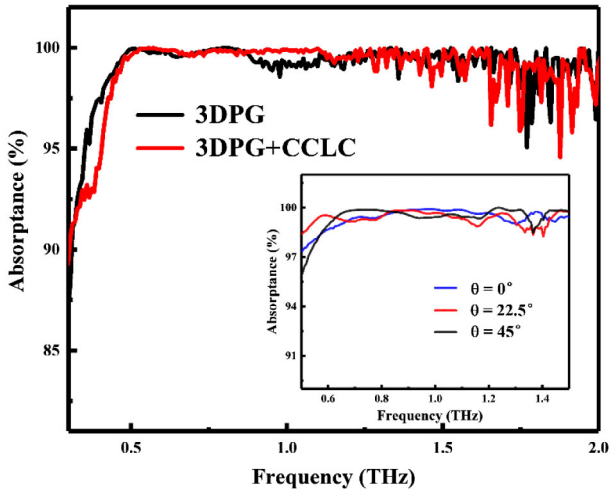

Fig. 2. THz absorptions of 3DPG embedded with CCLCs. Inset: at different incident angles.

conversion capacity, and good thermal conductivity, making it a promising candidate for high-efficiency THz thermal detection.

CLC is sometimes not stable. The encapsulation technique can be applied to overcome this issue [18]. A capsulized cholesteric liquid crystal (CCLC) has been used in various optical applications without requiring electricity or orientation alignment, including in flexible displays, secure authentication, and 3D omnidirectional microlasers [19]. Here, we design a new method for visualized detection of THz power based on the THz-photothermochromism of CCLC. Temperature-supersensitive CCLCs embedded 3DPG comprise the visual unit, while the 3DPG is also used as the THz absorption substrate. The color change of CCLCs under the incidence of high-power THz waves with different intensity is observed through a microscope system. The relationship between THz power and hue values of the CCLCs is obtained.

The configuration of the device is illustrated in Fig. 1(a). First, the CCLCs (RM2325, Japan Capsular Products) and silicone oil solvent are mixed, and then uniformly stirred using a magnetic stirrer. A small amount of the mixture is spin-coated onto the surface of the 3DPG. 3DPG absorbs THz radiation, which generates heat to produce the color change of the CCLCs. The 3DPG embedded with CCLCs, known as temperature-supersensitive thermal sensors, is shown by optical microscopy in Fig. 1(b). The CCLCs are randomly distributed within the porous graphene with different colors. The CCLCs exhibit different colors mainly because of different temperatures which means the microscopic temperature of porous graphene can be visually measured based on CCLCs [20]. The black background of 3DPG is favorable for the visible THz detection.

The 3DPG with CCLCs is characterized by scanning electron microscopy (SEM, Hitachi S-4800). The 3D graphene chemical vapor deposition (CVD) is grown using 3D metal foam as a template. Figure 1(c) shows that the diameter of the pores of the graphene is ∼200 μm and the CCLCs have an average diameter of 20 μm. The Raman spectrum of 3DPG is shown in Fig. 1(d), showing a very small intensity ratio of the D band to the G band, which is comparable to that of high-quality graphene. The G-to-2D peak intensity ratio is consistent with that observed for 3DPG [21].

The absorption curves of 3DPG and 3DPG embedded with CCLCs at normal incidence of THz waves are shown in Fig. 2 for the THz spectrum range from 0.25 to 2 THz. The absorption $A(\omega)$ is calculated as $1 - T(\omega) - R(\omega)$, where $T(\omega)$ and $R(\omega)$ are the transmittance and reflectance, measured by conventional THz time-domain spectroscopy. There is almost no reflection or transmission in the frequency range of 0.5–2 THz (not shown here), and the absorption of 3DPG without and with CCLCs was nearly the same, more than 95%. The 3D graphene has a porous structure with pores of several hundred micrometers, which is comparable to the THz wavelength shown in Fig. 1(c). This greatly reduces the reflection of incident THz waves from the surface of the graphene and enhances the interaction between the THz waves and graphene through multiple scattering within the graphene, resulting in near-perfect absorption and conversion into thermal energy to heat the CCLCs. So, the 3DPG is a very thin (∼0.5 mm thickness) but high-efficiency THz absorber. The absorption remains high with wide-angle incidence. The absorptance from 0.5 THz to 1.5 THz is shown for incident angle $\theta = 0°$, 22.5°, and 45° in the inset of Fig. 2. The added CCLCs do not reduce the THz absorption of 3DPG. The THz absorption of 3DPG with CCLCs is more than 98% in a continuous bandwidth of ∼1 THz. The jitters in the curves may be caused by the random distributions of the pores of the graphene and the CCLCs. From these results, the combination of CCLCs and 3DPG is a good candidate for THz thermal detection.

The setup for high-power THz generation and visible detection with CCLCs embedded in 3DPG is illustrated in Fig. 3(a). The irradiated broadband THz waves were generated by a pulse-front tilting method with a $LiNbO_3$ crystal pumped by a regeneratively amplified Ti: sapphire laser [22,23]. A black polypropylene filter is used to block the remaining pumped laser and the radiation produced in the crystal along with the THz generation. The THz source intensity is tunable by rotating the THz polarizer which is a commercial free-standing wire grid polarizer

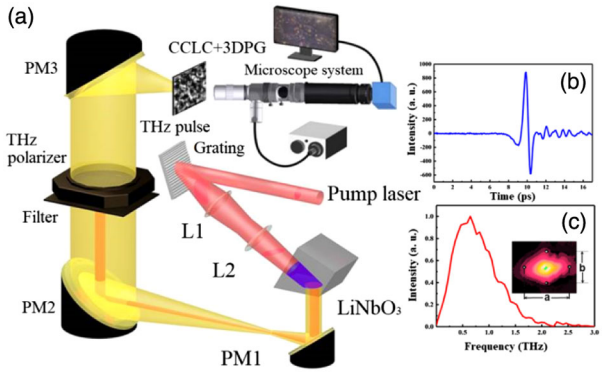

Fig. 3. Experimental setup. (a) Broadband THz waves are generated by the tilted-pump-pulse-front method using a $LiNbO_3$ crystal. The THz beam is tightly focused into the 3DPG-assisted CCLCs through off-axis parabolic mirrors (PMs). A visible microscope system is used for THz power measurement. (b) Measured THz temporal waveform and (c) its Fourier components. The inset shows the THz beam profile image at the focused point after PM3. $a = 940$ μm, $b = 587.5$ μm.

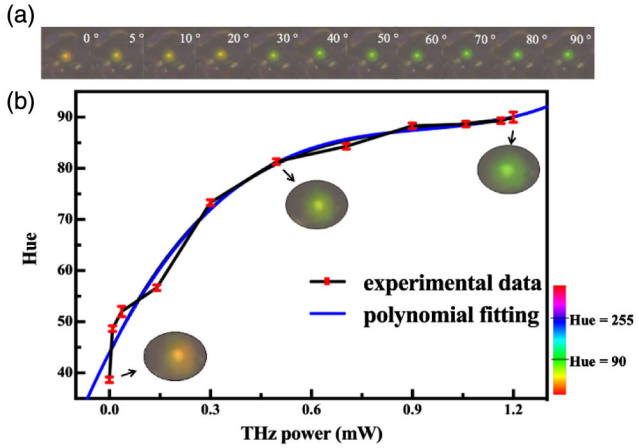

Fig. 4. (a) Visible pictures of a CCLC under different THz intensities under microscopy. (b) THz intensities' dependence of hue digitalized from the pictures of the CCLC. The images of the CCLC when the polarization angles are 0°, 40°, and 90° are shown.

(PUREWAVE). The 3DPG with CCLCs (1.5 cm × 1.5 cm) is placed at the focal point. THz radiation is normally incident on the sample. A microscopic system is used for measuring the images. It mainly consists of a CMOS camera (JC-HD200 S), an imaging lens (JC-TZ01), an auxiliary objective lens (JC-FZ10X), a computer, and a display. The pictures of CCLCs are taken by the microscopy imaging system with display and storage technology not only to make it convenient but also to ensure that the detection position is fixed. The computer was used for image processing. Figure 3(b) shows the THz temporal profile. Single-cycle THz pulses are generated by optical rectification from $LiNbO_3$ [24–26]. Due to the influence of water vapor absorption, the THz spectrum which is mainly 0–2 THz is not completely smooth, as shown in Fig. 3(c). The inset indicates that the THz beam spot size obtained by a THz camera (IRV-T0831C, NEC) has a spatial profile of a horizontal dimension of 940 μm and a vertical dimension of 587.5 μm after focusing by three off-axis parabolic mirrors (PMs). A commercial pyroelectric detector (THz-5B-MT, Gentec-EO) was used to calibrate the THz radiation power. The maximum average THz power (P_{max}) was 1.2 mW in our system. Thus, the maximum THz power density is as high as $2.8 \times 10^2 \mathrm{mW/cm^2}$. As the focused THz beam size is very small with a high power density, the heat generated by THz radiation in 3DPG can be applied to the CCLCs to achieve efficient visible detection.

To show the relationship between THz power and color change of CCLCs, we varied the power by rotating the THz polarizer to detect the color change of a CCLC microcapsule. When the angle of the wire grid polarizer $\theta = 0°$, which is parallel to the polarization of the THz wave, there is no THz transmission. The power maximum reaches 1.2 mW when $\theta = 90°$. As the THz power is increased with an interval of 10°, the color of the CCLC changes from orange to green under thermal equilibrium. Figure 4(a) shows the CCLC image taken by microscopy at room temperature, 21°C. We can see that the CCLC has corresponding responses with different THz powers. Image processing is necessary for evaluating the picture. We used Photoshop software to quantitatively visualize THz power based on hue value, which is widely used as an indicator of the color change [27,28]. The data from the image was processed using a 5 × 5 median pixel of the center point of the CCLC. The fitting curve obtained by fourth-order polynomials in Fig. 4(b) shows that hue increases monotonically with THz power. When the wire grid is rotated 5°, that is, the power of THz is only 0.009 mW (multiply P_{max} 1.2 mW by the square sine of the angle of 5°), a significant change in the color of the CCLC still can be clearly seen, which means that the detectable THz power sensitivity increases nearly an order of magnitude higher than in our previous work [13]. We do not take into account the insertion losses and extinction ratio of the THz polarizer. If we take these into consideration, the minimum detectable power could be even less than 0.009 mW. At high THz power, the curve becomes flat which is not expected. To get over limitations based on one CCLC, a multi-microcapsule analysis is used.

Seven CCLCs were chosen to visualize the THz power. Each point of Fig. 5(a) corresponds to a value of THz power which corresponds to an image in Fig. 5(b) (not shown all). And the point is the average of hue values of the seven CCLCs under the THz power. THz power dependence of hue digitalized from each CCLC is similar to Fig. 4(b). Because the CCLCs are randomly distributed in 3DPG, CCLCs may not be in the same horizonal plane, leading to some of their images at the focal plane while others are outside of the focal plane of our microscope system. But the blurring has no effect on the THz detection. A CCLC in a different zone may have a different response at the same temperature which means each individual CCLC may have a little different THz power detection. But once a CCLC is chosen, the result is the same which you can see in Fig. 4(b). With multi-microcapsule analysis, the relationship between THz power and the average hue values of seven CCLCs is improved to linear relation which is expected. One single CCLC is insufficient to visualize the THz power with high performance. Several CCLCs together can provide better results across the whole power range of the THz radiation (from low to high power). The THz source power is not so high that the temperature doesn't increase much. So, the CCLCs don't reach saturation (blue color). The maximum THz power detected and the dynamic range should be larger if large power THz source is measured.

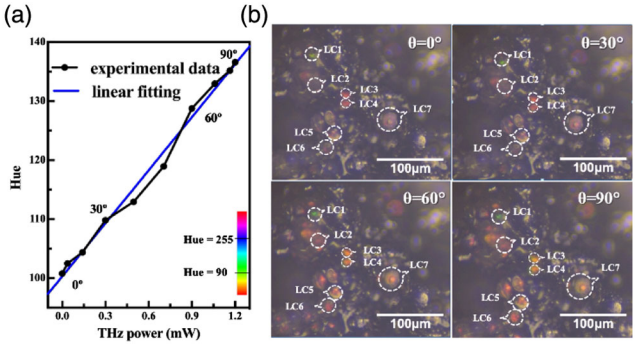

Fig. 5. (a) THz intensity dependence of the average hue digitized from the pictures of the seven CCLCs. (b) Images of the CCLCs under microscopy when the polarization angles are 0°, 30°, 60°, and 90°, respectively.

The flexible and freestanding 3DPG has the capabilities of broadband THz perfect absorption and excellent photothermal conversion, as well as black background. We first leverage temperature-supersensitive CCLCs embedded in 3DPG, the color change of which can be detected to visually measure THz power. Based on the hue value of a CCLC, we can visually obtain the THz power up to 2.8×10^2 mW/cm^2 with minimum detection limit 0.009 mW, which means the detection sensitivity is an order of magnitude higher than that reported in our previous work. Furthermore, by analyzing the average hues of multiple CCLCs, the relationship between THz power and hue value is improved to linearity, which is better for THz detection. Integrating metamaterials and optimizing porous graphene and CCLCs can allow detection of THz frequency and polarization and increase the sensitivity of the detector. The device reported here, which can convert THz radiation to visible light for detection at room temperature without additional electronic equipment, is simple, lightweight, and cheap, and can be used in a variety of situations, including alignment of THz systems, THz beam analysis, and THz sensing.

Funding. China Postdoctoral Science Foundation (2019M651768, 2020T130285); Fundamental Research Funds for the Central Universities (021314380095); Open Foundation Project of the National Laboratory of Solid State Microstructures, China; National Natural Science Foundation of China (61605088); JSPS KAKENHI (JP18H04515).

Acknowledgment. We thank the National Laboratory of Solid State Microstructures for the use of their equipment.

Disclosures. The authors declare no conflicts of interest.

REFERENCES

1. X. Zhang, A. Shkurinov, and Y. Zhang, Nat. Photonics **11**, 16 (2017).
2. M. Tonouchi, Nat. Photonics **1**, 97 (2007).
3. M. Hangyo, Jpn. J. Appl. Phys. **54**, 120101 (2015).
4. Y. Ji, F. Fan, S. Xu, J. Yu, Y. Liu, X. Wang, and S. Chang, Carbon **152**, 865 (2019).
5. NEC, "Terahertz imager," http://www.nec.com/en/global/prod/terahertz.
6. INO, "Microxcam-384i-THz terahertz camera," https://www.ino.ca/en/solutions/thz/microxcam-384i-thz/.
7. Ophir Optronics, "Pyrocam IIIHR beam profiling camera," http://www.ophiropt.com/laser–measurement/beam-profilers/products/Beam-Profiling/Camera-Profiling-with-BeamGage/Pyrocam-IIIHR.
8. Tydex, "Golay detectors," http://www.tydexoptics.com/products/thz_devices/golay_cell.
9. O. V. Chefonov, A. V. Ovchinikov, M. B. Agranat, and A. N. Stepanov, Opt. Lett. **44**, 4099 (2019).
10. F. Keilmann and K. F. Renk, Appl. Phys. Lett. **18**, 452 (1971).
11. I. Chen, S. Park, G. Chen, C. Wang, C. Bethea, R. Martini, and D. Woolard, Proc. SPIE **8624**, 862415 (2013).
12. Y. Tadokoro, T. Nishikawa, B.-Y. Kang, K. Takano, M. Hangyo, and M. Nakajima, Opt. Lett. **40**, 4456 (2015).
13. L. Wang, H. Qiu, T. N. K. Phan, K. Kato, B. Kang, K. Takano, Y. Lu, L. Chen, P. Lv, K. Yu, W. Wei, B. Jin, and M. Nakajima, Appl. Sci. **8**, 2580 (2018).
14. B. Kang, K. Takano, M. Nakajima, S.-B. Choi, D. Kim, and H. Lee, *42nd International Conference on Infrared, Millimeter, and Terahertz Waves (IRMMW-THz)*, Cancun, Mexico (IEEE, 2017).
15. Z. Huang, H. Chen, Y. Huang, Z. Ge, Y. Zhou, Y. Yang, P. Xiao, J. Liang, T. Zhang, Q. Shi, G. Li, and Y. Chen, Adv. Funct. Mater. **28**, 1704363 (2018).
16. S. Xu, F. Fan, J. Cheng, H. Chen, W. Ma, Y. Huang, and S. Chang, Adv. Opt. Mater. **7**, 1900555 (2019).
17. M. Chen, Y. Wang, J. Wen, H. Chen, W. Ma, F. Fan, Y. Huang, and Z. Zhao, ACS Appl. Mater. Interfaces **11**, 6411 (2019).
18. S. S. Lee and S.-H. Kim, Macromol. Res. **26**, 1054 (2018).
19. M. Schwartz, G. Lenzini, Y. Geng, P. B. Rønne, P. Y. A. Ryan, and J. P. F. Lagerwall, Adv. Mater. **30**, 1707382 (2018).
20. H. Jiang, Y. Tang, X. Zeng, R. Xiao, P. Lü, L. Wang, and Y. Lu, Chin. Opt. Lett. **18**, 031201 (2020).
21. H. Bi, I.-W. Chen, T. Lin, and F. Huang, Adv. Mater. **27**, 5943 (2015).
22. J. Hebling, K.-L. Yeh, M. C. Hoffmann, B. Bartal, and K. A. Nelson, J. Opt. Soc. Am. B **25**, B6 (2008).
23. H. Hirori, A. Doi, F. Blanchard, and K. Tanaka, Appl. Phys. Lett. **98**, 091106 (2011).
24. M. Nakajima, T. Kurihara, Y. Tadokoro, B. Kang, K. Takano, K. Yamaguchi, H. Watanabe, K. Oto, T. Suemoto, and M. Hangyo, J. Infrared Millim. Terahertz Waves **37**, 1199 (2016).
25. T. Kurihara, H. Watanabe, M. Nakajima, S. Karube, K. Oto, Y. Otani, and T. Suemoto, Phys. Rev. Lett. **120**, 107202 (2018).
26. S. Ohkoshi, K. Imoto, A. Namai, M. Yoshikiyo, S. Miyashita, H. Qiu, S. Kimoto, K. Kato, and M. Nakajima, J. Am. Chem. Soc. **141**, 1775 (2019).
27. J. L. Hay and D. K. Hollingsworth, Exp. Therm. Fluid Sci. **12**, 1 (1996).
28. J. Stasiek, A. Stasiek, M. Jewartowski, and M. W. Collins, Opt. Laser Technol. **38**, 243 (2006).